

Metal-Organic Frameworks

Electrically Conductive π -Intercalated Graphitic Metal-Organic Framework Containing Alternate π -Donor/Acceptor Stacks

Ashok Yadav, Shiyu Zhang, Paola A. Benavides, Wei Zhou, and Sourav Saha*

Abstract: Two-dimensional graphitic metal-organic frameworks (GMOF) often display impressive electrical conductivity chiefly due to efficient through-bond in-plane charge transport, however, less efficient out-of-plane conduction across the stacked layers creates large disparity between two orthogonal conduction pathways and dampens their bulk conductivity. To address this issue and engineer higher bulk conductivity in 2D GMOFs, we have constructed via an elegant bottom-up method the first π -intercalated GMOF (iGMOF1) featuring built-in alternate π -donor/acceptor (π -D/A) stacks of Cu^{II}-coordinated electron-rich hexaaminotriphenylene (HATP) ligands and non-coordinatively intercalated π -acidic hexacyano-triphenylene (HCTP) molecules, which facilitated out-of-plane charge transport while the hexagonal Cu₃(HATP)₂ scaffold maintained in-plane conduction. As a result, iGMOF1 attained an order of magnitude higher bulk electrical conductivity and much smaller activation energy than Cu₃(HATP)₂ ($\sigma = 25$ vs. 2 S m^{-1} , $E_a = 36$ vs. 65 meV), demonstrating that simultaneous in-plane (through-bond) and out-of-plane (through π D/A stacks) charge transport can generate higher electrical conductivity in novel iGMOFs.

Introduction

Electrically conductive metal-organic frameworks (MOFs)^[1–7] have emerged as one of the most sought functional materials due to their diverse potential applications in batteries,^[8–10] supercapacitors,^[11–15] transistors,^[16,17] chemiresistive sensors,^[18–24] and electrocatalysis^[25–31] that can help

advance modern electronics and energy technologies.^[32,33] To exhibit desired electrical conductivity, the MOFs must possess sufficient charge-carrier concentration and efficient long-range charge transport pathways.^[5] While redox-active building blocks and guest entities endow MOFs with necessary charge-carriers, creating well-defined efficient charge transport pathways through porous frameworks often proves challenging and requires innovative design strategies. Although 2D graphitic MOFs (GMOFs) composed of square-planar metal ions and trigonal-planar ligands often display impressive intrinsic conductivity chiefly due to efficient in-plane charge transport through metal-ligand coordination and conjugated π -bonds,^[34–48] out-of-plane conduction through the stacked hexagonal layers is much less efficient.^[45] The large disparity between the two orthogonal conduction pathways not only renders the conductivity of 2D GMOFs highly anisotropic, but also dampen their bulk conductivity. Although significant effort has been devoted to promoting in-plane, through-bond charge transport in 2D GMOFs by introducing different metal ions (Cu²⁺, Ni²⁺, and Co²⁺) and trigonal-planar hexa-substituted benzene and triphenylene ligands (HXB and HXTP, X = NH₂, OH, SH),^[34–48] the possibility and potential benefits of enhancing the out-of-plane charge transport capability of 2D GMOFs have been largely overlooked. Meanwhile, we and others have demonstrated that extended π -donor/acceptor (π -D/A) stacks featuring either mixed-valent ligands or redox-complementary ligands and intercalated guests facilitate through-space conduction and generate impressive electrical conductivity in 3D MOFs.^[49–60] Based on these observations, we envisioned that if installed in 2D GMOFs, alternate π -D/A stacks should promote out-of-plane charge transport while the 2D coordination network would maintain in-plane conduction (Figure 1), which should diminish the disparity between two orthogonal conduction pathways and boost their bulk conductivity. However, 2D GMOFs having alternate π -D/A stacks that can facilitate out-of-plane charge transport have not yet been developed possibly because narrow interlayer gaps ($\approx 3.2\text{--}3.5 \text{ \AA}$) render postsynthetic intercalation of redox-complementary π -systems between the GMOF layers practically impossible. This also underscores the need for a new bottom-up synthetic strategy that can give access to novel π -intercalated GMOFs (iGMOFs) and realize this unique possibility.

To construct such iGMOFs via a bottom-up method, the following conditions must be fulfilled: (1) the intercalating π -acceptors should not coordinate with the metal ions to form a separate complex or framework, nor should they interfere with the formation of GMOF scaffolds by π -donor

[*] Dr. A. Yadav, S. Zhang, P. A. Benavides, Prof. S. Saha
 Department of Chemistry, Clemson University
 Clemson, SC 29634 (USA)
 E-mail: souravs@clemson.edu

Dr. W. Zhou

NIST Center for Neutron Research, National Institute of Standards and Technology
 Gaithersburg, MD 20899 (USA)

© 2023 The Authors. Angewandte Chemie International Edition published by Wiley-VCH GmbH. This is an open access article under the terms of the Creative Commons Attribution Non-Commercial NoDerivs License, which permits use and distribution in any medium, provided the original work is properly cited, the use is non-commercial and no modifications or adaptations are made.

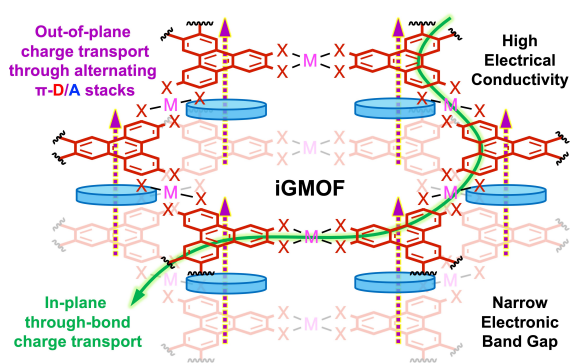


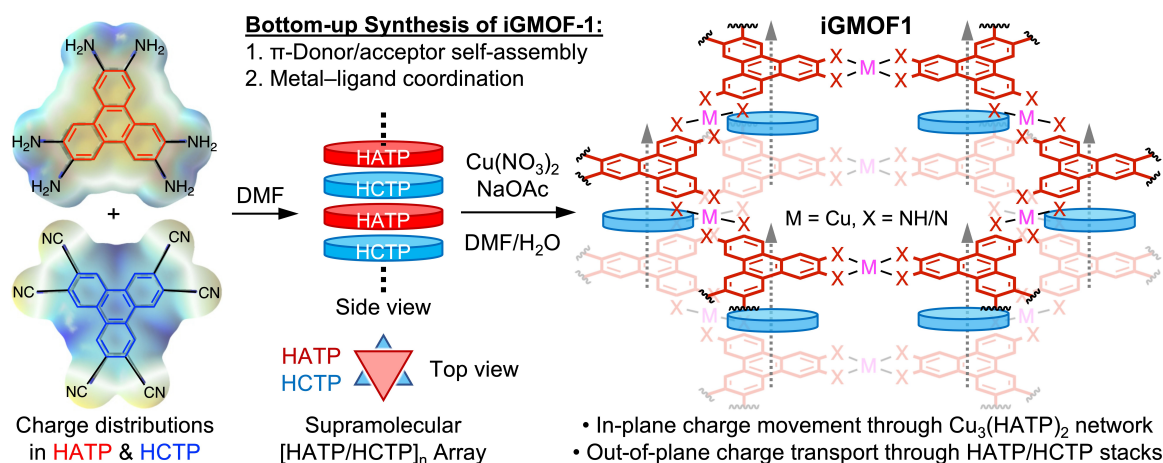
Figure 1. Graphical representation of dual in-plane (through-bond) and out-of-plane (through-space) conduction in iGMOF featuring alternate π -donor/acceptor stacks of metal-coordinated π -donor ligands and non-coordinatively intercalated π -acceptor molecules.

HXTP ligands, (2) the π -donor HXTP ligands of GMOF scaffolds and the non-coordinating π -acceptors should form robust alternate π -D/A arrays that must survive during subsequent GMOF scaffold formation in the presence of appropriate metal ions and become incorporated into the resulting iGMOFs, (3) the metal nodes of GMOF scaffolds should have square-planar geometry so that the non-coordinatively intercalated π -acceptor molecules remain sandwiched between the GMOF layers (in contrast, octahedral nodes with axially coordinated solvent molecules could sterically hinder the incorporation of preassembled π -D/A stacks), and (4) the GMOF scaffolds should be formed at moderate temperatures where the preassembled π -D/A arrays can easily survive and become incorporated into resulting iGMOFs. To fulfil all these criteria, we have employed a square-planar Cu^{2+} ion, a strong π -donor ligand, 2,3,6,7,10,11-hexaaminotriphenylene (HATP, HOMO: -4.3 eV), which forms 2D $\text{Cu}_3(\text{HATP})_2$ GMOF at room temperature, and a strong π -acceptor hexacyanotriphenylene (HCTP, LUMO: -3.7 eV), which forms a robust HATP/HCTP π -D/A array but does not coordinate with

Cu^{2+} nodes. This ideal combination yielded a novel iGMOF1 featuring 2D $\text{Cu}_3(\text{HATP})_2$ scaffold located in the ab-plane and built-in alternate π -D/A stacks of Cu^{2+} -coordinated HATP ligands and non-coordinatively intercalated HCTP molecules extended along the c -axis (Scheme 1). The iGMOF1 pellets consistently displayed an order of magnitude higher bulk electrical conductivity and much smaller thermal activation energy than pristine $\text{Cu}_3(\text{HATP})_2$ devoid of any intercalated π -acceptor ($\sigma_{\text{average}} \approx 25$ vs. 2 Sm^{-1} , $E_a = 36$ vs. 65 meV), which was attributed to more efficient out-of-plane charge transport through the built-in alternate HATP/HCTP stacks present in the former, as both materials possessed the same in-plane conduction pathways defined by the hexagonal $\text{Cu}_3(\text{HATP})_2$ network. This work not only unlocked the access to novel iGMOFs containing built-in alternate π -D/A stacks, but also demonstrated for the first time that improved out-of-plane charge transport through alternate π -D/A stacks, along with in-plane conduction through the coordination network can generate higher bulk electrical conductivity in 2D MOFs, delivering new design and synthesis strategies for electrically conductive MOFs.

Results and Discussion

A novel iGMOF1 containing built-in alternate π -D/A stacks of Cu^{2+} -coordinated HATP π -donor ligands and non-coordinatively intercalated HCTP π -acceptor guests was synthesized via an elegant bottom-up method involving self-assembly of an alternate $[\text{HATP}/\text{HCTP}]_n$ array, followed by selective coordination of HATP ligands with square-planar Cu^{2+} ions (Scheme 1). A mixture of light yellow colored DMF solutions of HATP and HCTP (in 1:1 molar ratio) immediately turned greenish brown indicating the formation of supramolecular $[\text{HATP}/\text{HCTP}]_n$ array, which upon slow solvent evaporation formed dark needle-shaped crystals suitable for single-crystal X-ray diffraction (SCXRD) analysis. Subsequent addition of an aqueous solution of Cu



Scheme 1. Bottom-up synthesis of novel iGMOF1 via self-assembly of supramolecular $[\text{HATP}/\text{HCTP}]_n$ π -D/A array, followed by Cu^{2+} -HATP coordination leading to the formation of 2D $\text{Cu}_3(\text{HATP})_2$ layers separated by non-coordinatively intercalated HCTP molecules.

(NO₃)₂·3H₂O (1.5 equiv of HATP) and NaOAc^[45] to the preassembled [HATP/HCTP]_n array solution in DMF at room-temperature yielded a microcrystalline black precipitate and the solution became colorless, indicating the formation of iGMOF1 [Cu₃(HATP)₂·(2HCTP)] featuring 2D hexagonal Cu₃(HATP)₂ layers located in the *ab*-planes and built-in alternate [HATP/HCTP]_n stacks extended along the *c*-axis (See Supporting Information for details). Although no such 2D iGMOF containing alternate π -D/A stacks has been constructed before, a similar two-step synthetic approach yielded a 2D π -intercalated covalent organic framework^[61] and a one-step self-assembly of a π -acidic tris-pyridyl-1,3,5-triazine ligand and π -donor triphenylene (TP) molecules in the presence of tetrahedral Zn^{II} ion yielded 3D coordination polymers containing alternate π -D/A stacks,^[62] portending the feasibility of our bottom-up approach to construct iGMOF1 having built-in π -D/A stacks.

To determine structure-composition-property relationships, we have also prepared pristine Cu₃(HATP)₂ under the same conditions (in the absence of HCTP) by mixing a HATP solution in DMF with an aqueous solution of Cu(NO₃)₂·3H₂O (2:3 molar ratio) and NaOAc at room temperature (see Supporting Information for details).^[45] In addition, a dark brown powder of supramolecular [HATP/HCTP]_n array was also isolated by adding Et₂O to its DMF solution. A control experiment confirmed that HCTP does not coordinate with Cu²⁺ to form any coordination complexes or MOFs, corroborating that the HCTP molecules of preassembled [HATP/HCTP]_n array became non-coordinatively intercalated between the Cu²⁺-coordinated HATP ligands of the Cu₃(HATP)₂ scaffold formed in the presence of Cu²⁺ without forming any unwanted complexes. Unlike square-planar Cu²⁺ ion, octahedral Co²⁺ and Ni²⁺ ions did not produce any analogous iGMOFs possibly because axially coordinated solvent molecules sterically prevented the HCTP molecules from remaining sandwiched between the HATP ligands during the MOF formation.^[34,45,48] Furthermore, π -donor molecules, such as pyrene and triphenylene

(TP) did not form any π -stacks with electron-rich HATP ligand, nor become intercalated between the Cu₃(HATP)₂ layers to form iGMOFs due to the lack of π -D/A interaction.

The SCXRD analysis of self-assembled [HATP/HCTP]_n array (Figure 2a)^[63] showed that alternate head-to-tail oriented HATP and HCTP molecules were stacked cofacially along the *c*-axis at short interplanar distances ($d_{\text{HATP/HCTP}} \approx 3.3$ Å), which indicated strong π -D/A interaction. Since the preassembled [HATP/HCTP]_n array was subsequently incorporated into microcrystalline iGMOF1, its SCXRD structure provided valuable insights into possible orientation of built-in HATP/HCTP stacks embedded in iGMOF1. The structure of microcrystalline iGMOF1 was elucidated by powder XRD (PXRD) analysis and computational modeling (Figure 2b–d). The experimental PXRD profile of iGMOF1 was in excellent agreement with the calculated pattern of its optimized structure, which confirmed its phase purity and ruled out the formation of any unwanted coordination networks. Like pristine Cu₃(HATP)₂, iGMOF1 also displayed prominent peaks (Figure S1) at $2\theta = 4.7^\circ$ and 9.5° corresponding to [100] facet's reflections, indicating long-range order in the *ab*-plane, which is defined by the hexagonal Cu₃(HATP)₂ layers present in both materials.^[45] iGMOF1 displayed additional peaks at $2\theta \approx 27.5^\circ$ corresponding to [001] facet's reflections, which was also found in preassembled [HATP/HCTP]_n array. These peaks indicated long-range order along the *c*-axis created by alternate HATP/HCTP stacks. Furthermore, Rietveld refinement of experimental PXRD data of iGMOF1 (Figure S2) based on its *in silico* generated optimized structure showed the best fit for a structure with an orthorhombic *C2mm* space group and unit cell parameters of $a = 21.82306$ Å, $b = 37.48085$ Å, and $c = 6.61066$ Å ($R_p = 5.6\%$, $R_{wp} = 7.2\%$), suggesting that it contains 2D hexagonal Cu₃(HATP)₂ layers located in the *ab*-planes and alternate π -D/A stacks of Cu-coordinated HATP ligands and non-coordinatively intercalated HCTP molecules extended along the *c*-axis. Scanning electron micrographs (SEM) revealed microcrystalline rod-like mor-

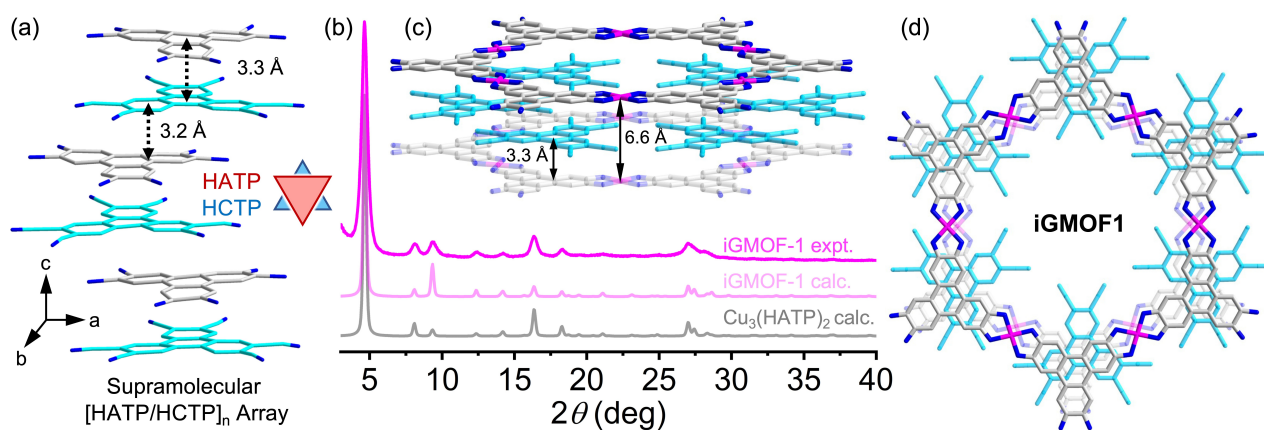


Figure 2. (a) Single-crystal structure of preassembled supramolecular alternate [HATP/HCTP]_n array. (b) The PXRD patterns of iGMOF1 (bright pink: experimental, faded pink: calculated based on the optimized structure) and pristine Cu₃(HATP)₂ (grey: calculated). (c, d) The calculated iGMOF1 structure featured eclipsed Cu₃(HATP)₂ layers separated by non-coordinatively intercalated HCTP molecules (cyan) at short interplanar distance ($d_{\text{HATP/HCTP}} \approx 3.3$ Å) suitable for strong π -donor/acceptor interactions and out-of-plane charge movement.

phology of both $\text{Cu}_3(\text{HATP})_2$ and iGMOF1 (Figure S3).^[45] These results demonstrated that the periodic structure of iGMOF1 was primarily defined by the 2D $\text{Cu}_3(\text{HATP})_2$ scaffold while the uncoordinated HCTP molecules sandwiched between the Cu-coordinated HATP ligands created alternate π -D/A stacks along the *c*-axis without disrupting its crystallinity and long-range order.

Furthermore, the optimized structure of iGMOF1 (Figure 2c, d) calculated by density functional theory (DFT) suggested that unlike pristine $\text{Cu}_3(\text{HATP})_2$, which contained slipped-parallel stacks with interlayer distance of $d_{\text{HATP}/\text{HATP}} \approx 3.2 \text{ \AA}$,^[45] the $\text{Cu}_3(\text{HATP})_2$ layers in iGMOF1 were fully eclipsed with twice as large interlayer distance ($d_{\text{Cu-Cu}}$ or $d_{\text{HATP-HATP}(\text{centroid})} \approx 6.6 \text{ \AA}$) and separated by the intercalated HCTP molecules ($d_{\text{HATP}/\text{HCTP}} \approx 3.3 \text{ \AA}$), which formed alternate $[\text{HATP}/\text{HCTP}]_n$ stacks along the *c*-axis. Like in precursor $[\text{HATP}/\text{HCTP}]_n$ array (Figure 2a), the cofacially stacked HATP and HCTP units of iGMOF1 were also oriented in head-to-tail fashion, suggesting that the pre-assembled HATP/HCTP arrays were seamlessly incorporated into iGMOF1 formed in the presence of Cu^{2+} . The intercalated HCTP molecules were slightly off-centered with respect to neighboring HATP ligands (centroid-centroid displacement $\approx 0.8 \text{ \AA}$), and its free CN-groups were projected toward the center of hexagonal channels of the $\text{Cu}_3(\text{HATP})_2$ scaffold. These structural features of iGMOF1 are well-suited for strong HATP/HCTP π -D/A interactions that can better facilitate out-of-plane charge transport along the *c*-axis.

FT-IR analysis of iGMOF1 (Figure S4) revealed the characteristic $\text{C}\equiv\text{N}$ stretching signal at 2240 cm^{-1} , confirming the presence of intercalated HCTP, which was not found in pristine $\text{Cu}_3(\text{HATP})_2$. The ^1H NMR spectra of self-assembled $[\text{HATP}/\text{HCTP}]_n$ array and iGMOF1 suspensions also showed the coexistence of characteristic HATP and HCTP signals (Figure S5a). Furthermore, the ^1H NMR spectrum of digested iGMOF1 displayed (Figure S5b) the characteristic signals of both HATP and HCTP ($\delta = 7.93$ and 9.44 ppm , respectively) with 1:1 integral ratio, confirming that the π -donor and acceptor units were present in equimolar ratio. In contrast, the ^1H NMR spectra of digested pristine and post-synthetically HCTP-treated $\text{Cu}_3(\text{HATP})_2$ (by soaking in a HCTP/DMF solution, see Supporting Information for details) displayed only characteristic HATP signal (Figure S5c), confirming that HCTP did not infiltrate into preformed $\text{Cu}_3(\text{HATP})_2$ due to short interlayer distances.

X-ray photoemission spectroscopy (XPS) analysis of iGMOF1 and $\text{Cu}_3(\text{HATP})_2$ (Figure S6) showed the characteristic Cu-2p ($\approx 933 \text{ eV}$) and N-1s ($\approx 399 \text{ eV}$) signals, but no sign of Na^+ (1071 eV), Cl^- (198 eV), and NO_3^- (407 eV) ions, confirming that both frameworks were charge neutral and devoid of any counterions. The deconvoluted high-resolution XPS of iGMOF1 (Figure 3a) revealed the characteristic Cu-2p_{3/2} (932.8 eV) and Cu-2p_{1/2} (952.7 eV) peaks accompanied by corresponding satellite peaks, which were also present in $\text{Cu}_3(\text{HATP})_2$ (Figure 3b), confirming that both materials contained only square-planar Cu^{2+} ions.^[45,64] In addition, the deconvoluted N-1s signal of iGMOF1

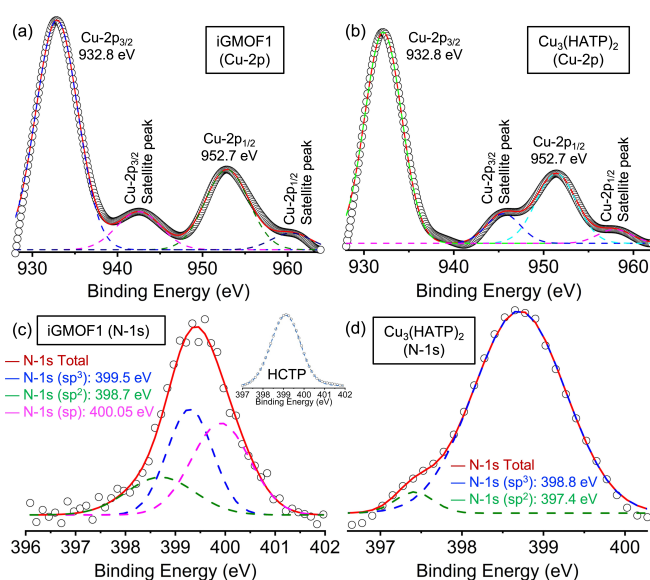


Figure 3. The deconvoluted high-resolution XPS data of iGMOF1 and $\text{Cu}_3(\text{HATP})_2$ show characteristic Cu^{2+} (a, b) and N-1s (c, d) signals. Open circles: observed, dotted lines: deconvoluted and fitted.

revealed (Figure 3c) three distinct peaks at 398.66, 399.45, and 400.05 eV : The first two peaks corresponded to imine- (N-sp^2) and amine- (N-sp^3) forms of HATP, respectively, which were also present in pristine $\text{Cu}_3(\text{HATP})_2$ (Figure 3d), whereas the third one belonged to sp -hybridized N atoms (CN) of intercalated HCTP,^[64] which pristine $\text{Cu}_3(\text{HATP})_2$ lacked. Thus, FT-IR, NMR, and XPS data confirmed the coexistence of HATP and HCTP in iGMOF1.

Thermogravimetric analysis (TGA) showed that (Figure S7) iGMOF1 lost ca. 5% weight until 80°C due to the loss of remaining solvent, and then maintained a stable plateau until ca. 300°C before decomposing completely at ca. 400°C . The residual weight of fully decomposed iGMOF1 (ca. 15%), which persisted until 1000°C , corresponded to CuO formed by the Cu^{2+} nodes, as all organic components disappeared as volatile CO_2 , H_2O , and N-oxide gases. This hypothesis was further supported by the fact that the precursor 1:1 $[\text{HATP}/\text{HCTP}]_n$ array (Figure S7) left no residual weight after its complete pyrolysis at ca. 450°C . The residual weight of thermally decomposed iGMOF1 was in excellent agreement with the unit formula of $[\text{Cu}_3(\text{HATP})_2 \cdot (2\text{HCTP})]$ having a formula weight of 1572, which produced three CuO molecules per unit ($\text{MW} = 79.5$; total 238.5 g of CuO in 1572 g of iGMOF1 $\approx 15 \text{ wt}\%$). In contrast, the TGA profiles of pristine and HCTP-treated $\text{Cu}_3(\text{HATP})_2$ (Figure S7) were quite similar, as both materials left ca. 22% residual weight corresponding to CuO formed upon complete thermal decomposition, which was consistent with a larger Cu-content in $\text{Cu}_3(\text{HATP})_2$ devoid of any HCTP than in iGMOF1 containing intercalated HCTP molecules.

The N_2 -sorption analysis (Figure S8) showed that evacuated iGMOF1 has a Brunauer–Emmett–Teller surface area (S_{BET}) of $154 \text{ m}^2 \text{ g}^{-1}$, which is roughly 80% of the S_{BET} of pristine $\text{Cu}_3(\text{HATP})_2$ ($195 \text{ m}^2 \text{ g}^{-1}$) prepared under the same conditions. Thus, the HCTP molecules sandwiched between

the Cu-coordinated HATP ligands stacked along the iGMOF1 walls did not significantly diminish its porosity. It also ruled out the possibility of HCTP molecules occupying the hexagonal channels of $\text{Cu}_3(\text{HATP})_2$ scaffold because such a scenario would have significantly diminished the material's porosity.

The UV-Vis-NIR absorption and diffuse-reflectance spectroscopies (DRS) further revealed HATP/HCTP π -D/A interaction in iGMOF1 as well as in the precursor array. Whereas beige colored HATP and HCTP did not absorb in the Vis-NIR region (Figure S9), the dark brown colored $[\text{HATP}/\text{HCTP}]_n$ array displayed prominent absorption peaks in the 500–1000 nm region stemming from π -D/A interactions.^[65,66] The DRS plots of iGMOF1 and its precursor $[\text{HATP}/\text{HCTP}]_n$ array also featured prominent bands in the 800–1400 nm region revealing HATP/HCTP π -D/A interaction, while pristine $\text{Cu}_3(\text{HATP})_2$ displayed a broad band in the 400–1000 nm region but no noticeable peak above 1000 nm (Figure 4a). The corresponding Tauc plots (Figure 4b) revealed that iGMOF1 enjoyed much narrower optical band gap than $\text{Cu}_3(\text{HATP})_2$ ($E_{\text{op}} = 0.8$ vs. 1.2 eV) due to better charge delocalization through alternate HATP/HCTP stacks present in the former.

The fact that both iGMOF1 and preassembled $[\text{HATP}/\text{HCTP}]_n$ array displayed the same characteristic optical signal of HATP/HCTP interaction further confirmed that the HCTP molecules remained sandwiched between the Cu-coordinated HATP ligands of iGMOF1 during the MOF formation and created built-in alternate π -D/A stacks. Had the HCTP molecules been somehow displaced from pre-assembled $[\text{HATP}/\text{HCTP}]_n$ array during the MOF formation and relocated inside the hexagonal $\text{Cu}_3(\text{HATP})_2$ channels, then the characteristic optical signals of HATP/HCTP array would not have persisted in resulting iGMOF1 and its S_{BET}

would have been significantly diminished. Thus, these results further supported the optimized iGMOF1 structure featuring alternate HATP/HCTP stacks embedded in its walls, which was also consistent with its experimental PXRD pattern.

Solid-state EPR studies shed additional light on the oxidation states of redox-active components of iGMOF1, $[\text{HATP}/\text{HCTP}]_n$ array, and $\text{Cu}_3(\text{HATP})_2$ (Figure 4c and d). Both iGMOF1 and pristine $\text{Cu}_3(\text{HATP})_2$ displayed characteristic EPR signals of paramagnetic Cu^{2+} ions at $g = 2.17$ and 2.03.^[45] Furthermore, iGMOF1 and its precursor $[\text{HATP}/\text{HCTP}]_n$ array displayed characteristic signals of organic radicals at $g = 2.001$, revealing the presence of $\text{HATP}^{\bullet+}/\text{HCTP}^{\bullet-}$ radical ion pair.^[65]

Cyclic voltammetric (CV) studies also revealed HATP/HCTP interaction inside iGMOF1 (Figure S10). While free HATP ligand underwent reversible first oxidation at +0.49 V (anodic peak, vs. Ag/AgCl) and free HCTP experienced quasi-reversible first reduction at -0.80 V (cathodic peak, vs. Ag/AgCl), in supramolecular $[\text{HATP}/\text{HCTP}]_n$ array, the first oxidation of HATP (+0.58 V, anodic peak) and the first reduction of HCTP (-0.97 V, cathodic peak) required higher applied potentials due to π -D/A interactions. The solid-state CV of iGMOF1 also showed that the first oxidation of HATP (+0.60 V, anodic peak) and the first reduction of HCTP (-1.1 V, cathodic peak) took place at even higher applied potentials, confirming that HATP/HCTP interaction persisted in iGMOF1.

Finally, to determine the effects of out-of-plane charge transport capability of alternate HATP/HCTP stacks embedded in iGMOF1, we compared electrical conductivities of iGMOF1 and pristine $\text{Cu}_3(\text{HATP})_2$ pellets measured by standard two-probe method.^[55,56,67] Both materials displayed linear current-voltage (I - V) relationships (Figure 5a) indicating ohmic conduction. Gratifyingly, the bulk conductivity of iGMOF1 ($\sigma_{\text{highest}} = 30 \text{ S m}^{-1}$, $\sigma_{\text{average}} = 25 (\pm 5) \text{ S m}^{-1}$) was consistently an order of magnitude greater than that of $\text{Cu}_3(\text{HATP})_2$ ($\sigma_{\text{highest}} = 2.7 \text{ S m}^{-1}$, $\sigma_{\text{average}} = 2.1 (\pm 0.5) \text{ S m}^{-1}$) prepared and measured under the same conditions (295 K). Since both materials possessed the same in-plane conduction pathways defined by hexagonal $\text{Cu}_3(\text{HATP})_2$ coordination network, the higher bulk conductivity of iGMOF1 was attributed to more efficient out-of-plane conduction through alternate HATP/HCTP stacks located along its c -axis (Figure 1), which pristine $\text{Cu}_3(\text{HATP})_2$ lacked. Furthermore, electrical conductivity of iGMOF1 was $> 10^6$ times higher than that of supramolecular $[\text{HATP}/\text{HCTP}]_n$ array ($1.8 \times 10^{-5} \text{ S m}^{-1}$), which lacked through-bond charge transport capacity. These comparisons demonstrated that both in-plane and out-of-plane conduction contributed to a considerably higher bulk conductivity of iGMOF1. In contrast, the pellet conductivity of post-synthetically HCTP-treated $\text{Cu}_3(\text{HATP})_2$ was comparable to that of pristine $\text{Cu}_3(\text{HATP})_2$ (3.9 S m^{-1} , Figure 5a) because HCTP did not permeate into pre-made $\text{Cu}_3(\text{HATP})_2$, which was also indicated by the NMR and TGA data (see above).

While iGMOF1 pellets displayed an impressive bulk conductivity, which was on par with other highly conductive MOFs, the pellet conductivity values of MOFs are often few

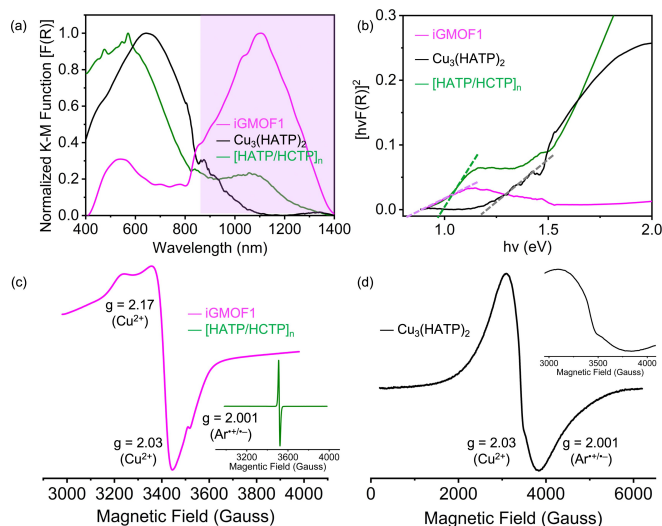


Figure 4. (a) UV-Vis-NIR DRS and (b) Tauc plots of pristine $\text{Cu}_3(\text{HATP})_2$ (black), iGMOF1 (pink), supramolecular $[\text{HATP}/\text{HCTP}]_n$ array (green) show π -donor/acceptor interactions and optical band gaps. The EPR spectra of (c) iGMOF1 and supramolecular $[\text{HATP}/\text{HCTP}]_n$ array (inset) and (d) pristine $\text{Cu}_3(\text{HATP})_2$ (inset: expanded) show the presence of paramagnetic Cu^{2+} and aromatic radicals ($\text{Ar}^{\bullet+}/\text{Ar}^{\bullet-}$).

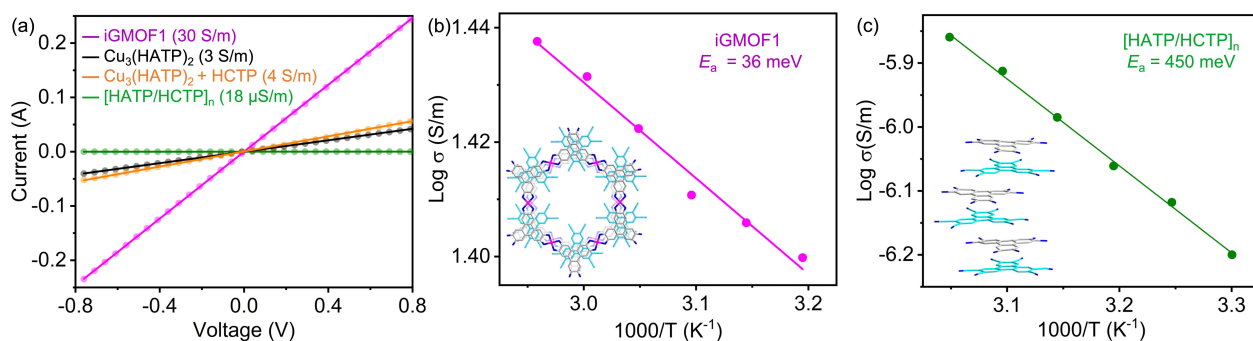


Figure 5. (a) Representative I - V plots of iGMOF1 (pink), $\text{Cu}_3(\text{HATP})_2$ (black: pristine, orange: HCTP-treated), and supramolecular $[\text{HATP}/\text{HCTP}]_n$ array (green). Arrhenius plots of temperature-dependent electrical conductivities of (b) iGMOF1 and (c) $[\text{HATP}/\text{HCTP}]_n$ precursor array.

orders of magnitude lower than single-crystal conductivity (if/when such measurements are possible) due to the contribution of grain-boundary resistance in the former,^[5,45,68] suggesting that the conductivity of iGMOF1 could actually be even higher if large enough crystals suitable for such measurements were available. In our hands, the pellet conductivity values of pristine $\text{Cu}_3(\text{HATP})_2$ prepared under the same conditions as iGMOF1 and also according to literature protocols were consistently an order of magnitude lower than the reported values (Figure S11).^[18,45] This is not uncommon for conductive MOFs, as different synthesis and measurement conditions often cause such variations.^[5,67]

The Arrhenius plots of temperature-dependent electrical conductivities (Figure 5b, c and S12) showed that iGMOF1 enjoyed much lower thermal activation energy ($E_a = 36$ meV) than pristine $\text{Cu}_3(\text{HATP})_2$ (65 meV)^[45] and $[\text{HATP}/\text{HCTP}]_n$ array (450 meV). The temperature-dependent PXRD of iGMOF1 (Figure S13) demonstrated that its crystalline structure remained intact at least up to 100 °C. Since both iGMOF1 and $\text{Cu}_3(\text{HATP})_2$ possessed the same in-plane charge-transport pathways defined by the Cu^{II} -HATP coordination network, the higher bulk conductivity and lower activation energy of the former are attributed to improved out-of-plane charge transport through alternate HATP/HCTP stacks, which the latter lacked.

When π -donors, such as pyrene and TP were introduced instead of π -acceptor HCTP during the MOF synthesis, they did not intercalate between electron-rich HATP ligands, nor yielded any analogous iGMOFs due to the lack of complementary π -D/A interaction (see Supporting Information for details). The PXRD and TGA profiles of resulting black microcrystalline powders formed in the presence of these π -donors resembled that of pristine $\text{Cu}_3(\text{HATP})_2$ (Figures S14 and S15), while the ¹H NMR spectra of the digested materials (Figure S16) revealed the presence of only HATP but no pyrene or TP. Consequently, the conductivities of $\text{Cu}_3(\text{HATP})_2$ formed in the presence of pyrene and TP (2.5 ± 0.5 and 3.4 ± 0.7 S m^{-1} , respectively, Figure S17) were comparable to that of pristine $\text{Cu}_3(\text{HATP})_2$ because the excluded π -donors had no effect on its conductivity. These control studies further underscored the importance of π -D/

A interaction on bottom-up synthesis of iGMOF1, as well as its improved out-of-plane charge transport capability, which led to a higher bulk conductivity.

To gain further insights into π -D/A interaction in precursor $[\text{HATP}/\text{HCTP}]_n$ array and the charge transport pathways in iGMOF1, we calculated their frontier molecular orbitals, electronic band structures, and density-of-states (DOS) by DFT. The frontier orbitals of HATP/HCTP complex calculated by applying the structural constraints of its SCXRD structure revealed that the highest-occupied and lowest-unoccupied molecular orbitals (HOMO and LUMO) were located on π -donor HATP and π -acceptor HCTP, respectively (Figure 6a), which is a characteristic feature of π -D/A interaction. Consistent with its experimentally observed semiconducting nature, i.e., thermally activated conduction, the calculated electronic band structure of iGMOF1 (Figure 6b left panel, see Supporting Information for details) showed well-dispersed valence and conduction bands on opposite sides of the Fermi level but none formally crossing it. The valence band maximum (VBM) of iGMOF1 in the out-of-plane (S - R) direction of Brillouin zone diagram (Figure 6c) resided only ≈ 30 meV below the Fermi level and approached the conduction band minimum (CBM) located just across the Fermi level, creating a very narrow electronic band gap (< 100 meV) due to facile out-of-plane charge transport along the c -axis. Furthermore, the VBM of iGMOF1 is dispersed by 200–400 meV along in-plane Z - T , Γ - Y , Γ - S , and R - Z directions, indicating efficient through-bond conduction within the ab -plane. Furthermore, the DOS of iGMOF1 (Figure 6b right panel) reveals that its VBM and CBM consist of Cu - $3d$, HATP and HCTP (N - $2p$ and C - $2p$) orbitals. The contributions of Cu - $3d$ and HATP- $2p$ orbitals indicated through-bond conduction within ab -plane,^[67,69,70] while that of non-coordinatively intercalated HCTP- $2p$ orbitals indicated its involvement in out-of-plane charge transport through alternate HATP/HCTP stacks along the c -axis.

Although these computational results were consistent with the experimentally observed semiconducting behavior of iGMOF1 and provided valuable insights into its charge transport pathways, it is important to note that band structure calculations of MOFs containing non-coordinated guest molecules are far more challenging than of pristine

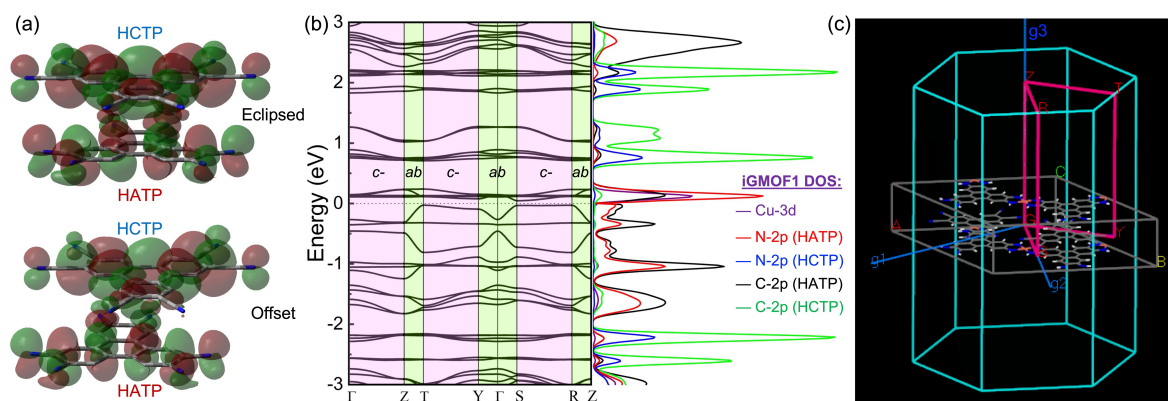


Figure 6. (a) The HOMO–LUMO diagrams of HATP/HCTP array with fully eclipsed and offset orientations (B3LYP/6-31G(d)). (b) The calculated electronic band structure (left) and DOS (right) of iGMOF1 show a narrow (< 100 meV) band gap and orbital contributions of participating elements to its valence and conduction bands. (c) Brillouin zone diagram shows in-plane and out-of-plane charge transport directions in iGMOF1.

MOFs devoid of any intercalated guest molecules. Therefore, although iGMOF1 exhibited 10-times higher conductivity and lower thermal activation energy than pristine $\text{Cu}_3(\text{HATP})_2$, which are consistent with its semiconducting nature, the latter apparently possesses electronic bands crossing the Fermi level in both *ab*- and *c*-directions (Figure S18) indicating a metallic behavior^[71] despite exhibiting thermally activated conduction, i.e., a semiconducting feature.^[45] Therefore, additional computational studies based on more sophisticated (also more time and resource consuming) structural models could better account for the complex effects of alternate HATP/HCTP stacks present in iGMOF1 and depict a more accurate picture of its two orthogonal conduction pathways.

Conclusion

In summary, to minimize the disparity between more efficient through-bond in-plane charge transport and modest through-space out-of-plane conduction pathways in 2D graphitic MOFs, which renders their conductivity highly anisotropic and somewhat dampens bulk conductivity, we have developed the first complementary π -intercalated graphitic MOF containing alternate π -donor/acceptor stacks of Cu^{2+} -coordinated HATP ligands and non-coordinatively intercalated HCTP molecules extended along the *c*-axis, which facilitated out-of-plane conduction while the Cu_3 -(HATP)₂ scaffold enabled in-plane charge transport. Since post-synthetic intercalation of π -acceptor units between tightly stacked layers of pre-made $\text{M}_3(\text{HATP})_2$ MOFs is not practically feasible, iGMOF1 containing built-in alternate HATP/HCTP was synthesized by a bottom-up method involving self-assembly of $[\text{HATP}/\text{HCTP}]_n$ array, followed by the formation of $\text{Cu}_3(\text{HATP})_2$ scaffold via Cu^{2+} –HATP coordination. Simultaneous in-plane through-bond and out-of-plane through HATP/HCTP stack conduction helped create impressive bulk conductivity (25 Sm^{-1}) in iGMOF1, which was an order of magnitude higher than that of pristine $\text{Cu}_3(\text{HATP})_2$ MOF and on par with highly conductive MOFs

developed to date. Thus, this work presents new design and bottom-up synthetic strategies that unlocked the access to unique π -intercalated graphitic MOFs containing alternate π -donor/acceptor stacks that can promote out-of-plane charge transport and generate higher bulk conductivity. This new paradigm will help advance electrically conductive MOFs and render them applicable in molecular electronics and energy technologies.

Acknowledgements

This work was supported by the US National Science Foundation (award nos. DMR-1809092 and CHE-2203985). The DFT calculations were performed on the NIST Enki HPC cluster and Clemson University Palmetto Cluster computing facilities.

Conflict of Interest

The authors declare no conflict of interest.

Data Availability Statement

The data that support the findings of this study are available in the supplementary material of this article.

Keywords: Bottom-up Synthesis · Electrical Conductivity · Graphitic Metal–Organic Frameworks · π -Donor/Acceptor Interaction · π -Intercalation

- [1] M. Jacoby, *C&EN* **2021**, 99, 30–34.
- [2] L. Sun, M. G. Campbell, M. Dincă, *Angew. Chem. Int. Ed.* **2016**, 55, 3566–3579.
- [3] C. F. Leong, P. M. Usov, D. M. D'Alessandro, *MRS Bull.* **2016**, 41, 858–864.

- [4] M. Ko, L. Mendecki, K. A. Mirica, *Chem. Commun.* **2018**, 54, 7873–7891.
- [5] L. S. Xie, G. Skorupskii, M. Dincă, *Chem. Rev.* **2020**, 120, 8536–8580.
- [6] M. Wang, R. Dong, X. Feng, *Chem. Soc. Rev.* **2021**, 50, 2764–2793.
- [7] E. Johnson, S. Ilic, A. J. Morris, *ACS Cent. Sci.* **2021**, 7, 445–453.
- [8] H. Wang, Q.-L. Zhu, R. Zou, Q. Xu, *Chem* **2017**, 2, 52–80.
- [9] K. W. Nam, S. S. Park, R. dos Reis, V. P. Dravid, H. Kim, C. A. Mirkin, J. F. Stoddart, *Nat. Commun.* **2019**, 10, 4948.
- [10] X. Wen, Q. Zhang, J. Guan, *Coord. Chem. Rev.* **2020**, 409, 213214.
- [11] L. Wang, Y. Z. Han, X. Feng, J. W. Zhou, P. F. Qi, B. Wang, *Coord. Chem. Rev.* **2016**, 307, 361–381.
- [12] G. Xu, P. Nie, H. Dou, B. Ding, L. Li, X. Zhang, *Mater. Today* **2017**, 20, 191–209.
- [13] D. Sheberla, J. C. Bachman, J. S. Elias, C.-J. Sun, Y. Shao-Horn, M. Dincă, *Nat. Mater.* **2017**, 16, 220–224.
- [14] W.-H. Li, K. Ding, H.-R. Tian, M.-S. Yao, B. Nath, W.-H. Deng, Y. Wang, G. Xu, *Adv. Funct. Mater.* **2017**, 27, 1702067.
- [15] H. Wu, W. Zhang, S. Kandambeth, O. Shekha, M. Eddaoudi, H. N. Alshareef, *Adv. Energy Mater.* **2019**, 9, 1900482.
- [16] G. Wu, J. Huang, Y. Zang, J. He, G. Xu, *J. Am. Chem. Soc.* **2017**, 139, 1360–1363.
- [17] B. Wang, Y. Luo, B. Liu, G. Duan, *ACS Appl. Mater. Interfaces* **2019**, 11, 35935–35940.
- [18] M. G. Campbell, D. Sheberla, S. F. Liu, T. M. Swager, M. Dincă, *Angew. Chem. Int. Ed.* **2015**, 54, 4349–4352.
- [19] M. G. Campbell, S. F. Liu, T. M. Swager, M. Dincă, *J. Am. Chem. Soc.* **2015**, 137, 13780–13783.
- [20] M.-S. Yao, X.-J. Lv, Z.-H. Fu, W.-H. Li, W.-H. Deng, G.-D. Wu, G. Xu, *Angew. Chem. Int. Ed.* **2017**, 56, 16510–16514.
- [21] V. Rubio-Giménez, N. Almora-Barrios, G. Escorcía-Ariza, M. Galbati, M. Sessolo, S. Tatay, C. Marti-Gastaldo, *Angew. Chem. Int. Ed.* **2018**, 57, 15086–15090.
- [22] M. L. Aubrey, M. T. Kapelewski, J. F. Melville, J. Oktawiec, D. Presti, L. Gagliardi, J. R. Long, *J. Am. Chem. Soc.* **2019**, 141, 5005–5013.
- [23] M.-S. Yao, J.-J. Zheng, A.-Q. Wu, G. Xu, S. S. Nagarkar, G. Zhang, M. Tsujimoto, S. Sakaki, S. Horike, K. Otake, S. Kitagawa, *Angew. Chem. Int. Ed.* **2020**, 59, 172–176.
- [24] W.-T. Koo, J.-S. Jang, I.-D. Kim, *Chem* **2019**, 5, 1938–1963.
- [25] A. J. Clough, J. W. Yoo, M. H. Mecklenburg, S. C. Marinescu, *J. Am. Chem. Soc.* **2015**, 137, 118–121.
- [26] E. M. Miner, T. Fukushima, D. Sheberla, L. Sun, Y. Surendranath, M. Dincă, *Nat. Commun.* **2016**, 7, 10942.
- [27] S. Lin, Y. Pineda-Galvan, W. A. Maza, C. C. Epley, J. Zhu, M. C. Kessinger, Y. Pushkar, A. J. Morris, *ChemSusChem* **2017**, 10, 514–522.
- [28] C. A. Downes, S. C. Marinescu, *ChemSusChem* **2017**, 10, 4374–4392.
- [29] C. A. Downes, A. J. Clough, K. Chen, J. W. Yoo, S. C. Marinescu, *ACS Appl. Mater. Interfaces* **2018**, 10, 1719–1727.
- [30] E. M. Miner, L. Wang, M. Dincă, *Chem. Sci.* **2018**, 9, 6286–6291.
- [31] J. D. Yi, D. H. Shi, R. Xie, Q. Yin, M. D. Zhang, Q. Wu, G. L. Chai, Y. B. Huang, R. Cao, *Angew. Chem. Int. Ed.* **2021**, 60, 17108–17114.
- [32] Stassen, N. Burtch, A. Talin, P. Falcaro, M. Allendorf, R. Ameloot, *Chem. Soc. Rev.* **2017**, 46, 3185–3241.
- [33] M. Allendorf, R. Dong, X. Feng, S. Kaskel, D. Matoza, V. Stavila, *Chem. Rev.* **2020**, 120, 8581–8640.
- [34] M. Hmadeh, Z. Lu, Z. Liu, F. Gándara, H. Furukawa, S. Wan, V. Augustyn, R. Chang, L. Liao, F. Zhou, E. Perre, V. Ozolins, K. Suenaga, X. Duan, B. Dunn, Y. Yamamoto, O. Terasaki, O. M. Yaghi, *Chem. Mater.* **2012**, 24, 3511–3513.
- [35] D. Sheberla, L. Sun, M. A. Blood-Forsythe, S. Er, C. R. Wade, C. K. Brozek, A. Aspuru-Guzik, M. Dincă, *J. Am. Chem. Soc.* **2014**, 136, 8859–8862.
- [36] T. Kambe, R. Sakamoto, T. Kasumato, T. Pal, N. Fukui, K. Hoshiko, T. Shimojima, Z. Wang, T. Hirahara, K. Ishizaka, S. Hasegawa, F. Liu, H. Nishihara, *J. Am. Chem. Soc.* **2014**, 136, 14357–14360.
- [37] J. Cui, Z. Xu, *Chem. Commun.* **2014**, 50, 3986–3988.
- [38] X. Huang, P. Sheng, Z. Tu, F. Zhang, J. Wang, H. Geng, Y. Zou, C. Di, Y. Yi, Y. Sun, W. Xu, D. Zhu, *Nat. Commun.* **2015**, 6, 7408.
- [39] H. Dou, L. Sun, Y. Ge, W. Li, C. H. Hendon, J. Li, S. Gul, J. Yano, E. A. Stach, M. Dincă, *J. Am. Chem. Soc.* **2017**, 139, 13608–13611.
- [40] A. J. Clough, J. M. Skelton, C. A. Downes, A. A. De La Rosa, J. W. Yoo, A. Walsh, B. C. Melot, S. C. Marinescu, *J. Am. Chem. Soc.* **2017**, 139, 10863–10867.
- [41] N. Lahiri, N. Lotfizadeh, R. Tsuchikawa, V. V. Deshpande, J. Louie, *J. Am. Chem. Soc.* **2017**, 139, 19–22.
- [42] R. Dong, P. Han, H. Arora, M. Ballabio, M. Karakus, Z. Zhang, C. Shekhar, P. Adler, P. S. Petkov, A. Erbe, S. C. B. Mannsfeld, C. Felser, T. Heine, M. Bonn, Z. Feng, E. Cánovas, *Nat. Mater.* **2018**, 17, 1027–1032.
- [43] E. Ziebel, L. E. Darago, J. R. Long, *J. Am. Chem. Soc.* **2018**, 140, 3040–3051.
- [44] A. J. Clough, N. M. Orchanian, J. M. Skelton, A. J. Neer, S. A. Howard, C. A. Downes, L. F. J. Piper, A. Walsh, B. C. Melot, S. C. Marinescu, *J. Am. Chem. Soc.* **2019**, 141, 16323–16330.
- [45] T. Chen, J.-H. Dou, L. Yang, C. Sun, N. Libretto, G. Skorupskii, J. T. Miller, M. Dincă, *J. Am. Chem. Soc.* **2020**, 142, 12367–12373.
- [46] R. W. Day, D. K. Bediako, M. Rezaee, L. R. Parent, G. Skorupskii, M. Q. Arguilla, C. H. Hendon, I. Stassen, N. Gianneschi, P. Kim, M. Dincă, *ACS Cent. Sci.* **2019**, 5, 1959–1964.
- [47] D.-G. Ha, M. Rezaee, Y. Han, S. A. Siddiqui, R. W. Day, L. S. Xie, B. J. Modtland, D. A. Muller, J. Kong, P. Kim, M. Dincă, M. A. Baldo, *ACS Cent. Sci.* **2021**, 7, 104–109.
- [48] J.-H. Dou, M. Q. Arguilla, Y. Luo, J. Li, W. Zhang, L. Sun, J. L. Mancuso, L. Yang, T. Chen, L. R. Parent, G. Skorupskii, N. J. Libretto, C. Sun, J. T. Miller, J. Kong, C. H. Hendon, J. Sun, M. Dincă, *Nat. Mater.* **2021**, 20, 222–228.
- [49] S. S. Park, E. R. Hontz, L. Sun, C. H. Hendon, A. Walsh, T. Van Voorhis, M. Dincă, *J. Am. Chem. Soc.* **2015**, 137, 1774–1777.
- [50] S. Xie, E. V. Alexandrov, G. Skorupskii, D. M. Proserpio, M. Dincă, *Chem. Sci.* **2019**, 10, 8558–8565.
- [51] G. Skorupskii, B. A. Trump, T. W. Kasel, C. M. Brown, C. H. Hendon, M. Dincă, *Nat. Chem.* **2020**, 12, 131–136.
- [52] G. Skorupskii, K. N. Le, D. M. L. Cordova, L. Yang, T. Chen, C. H. Hendon, M. Q. Arguilla, M. Dincă, *Proc. Natl. Acad. Sci. USA* **2022**, 119, e2205127119.
- [53] Z. Guo, D. K. Panda, K. Maity, D. Lindsey, T. G. Parker, T. E. Albrecht-Schmitt, J. L. Barreda-Esparza, P. Xiong, W. Zhou, S. Saha, *J. Mater. Chem. C* **2016**, 4, 894–899.
- [54] Z. Guo, D. K. Panda, M. A. Gordillo, A. Khatun, H. Wu, W. Zhou, S. Saha, *ACS Appl. Mater. Interfaces* **2017**, 9, 32413–32417.
- [55] M. A. Gordillo, P. A. Benavides, D. K. Panda, S. Saha, *ACS Appl. Mater. Interfaces* **2020**, 12, 12955–12961.
- [56] S. Zhang, D. K. Panda, A. Yadav, W. Zhou, S. Saha, *Chem. Sci.* **2021**, 12, 13379–13391.
- [57] S. Goswami, D. Ray, K. Otake, C.-W. Kung, S. J. Garibay, T. Islamoglu, A. Atilgan, Y. Cui, C. J. Cramer, O. K. Farha, J. T. Hupp, *Chem. Sci.* **2018**, 9, 4477–4482.
- [58] A. M. Rice, E. A. Dolgoplova, B. J. Yarbrough, G. A. Leith, C. M. Martin, K. S. Stephenson, R. A. Heugh, A. M. Brandt,

- D. A. Chen, S. G. Karakalos, M. D. Smith, K. B. Hatzell, P. J. Pellechia, S. Garashchuk, N. B. Shustova, *Angew. Chem. Int. Ed.* **2018**, *57*, 11310–11315.
- [59] D. Ukaj, H. Bunzen, J. Berger, G. Kieslich, R. A. Fischer, *Chem. Mater.* **2021**, *33*, 2532–2542.
- [60] J. Su, N. Xu, R. Murase, Z.-M. Yang, D. M. D'Alessandro, J.-L. Zuo, J. Zhu, *Angew. Chem. Int. Ed.* **2021**, *60*, 4789–4795.
- [61] H. Li, P. Shao, S. Chen, G. Li, X. Feng, X. Chen, H.-J. Zhang, J. Lin, Y.-B. Jiang, *J. Am. Chem. Soc.* **2020**, *142*, 3712–3717.
- [62] M. Kawano, T. Kawamichi, T. Haneda, T. Kojima, M. Fujita, *J. Am. Chem. Soc.* **2007**, *129*, 15418–15419.
- [63] Deposition number 2173152 (for [HATP/HCTP]_n array) contains the supplementary crystallographic data for this paper. These data are provided free of charge by the joint Cambridge Crystallographic Data Centre and Fachinformationszentrum Karlsruhe Access Structures service.
- [64] J. Chastain, R. C. King Jr., *Handbook of X-ray Photoelectron Spectroscopy, Vol. 40*, Perkin–Elmer Corporation, **1992**, pp. 221.
- [65] S. V. Rosokha, J. K. Kochi, *Acc. Chem. Res.* **2008**, *41*, 641–653.
- [66] P. M. Alvey, J. J. Reczek, V. Lynch, B. L. Iverson, *J. Org. Chem.* **2010**, *75*, 7682–7690.
- [67] A. Yadav, D. K. Panda, S. Zhang, W. Zhou, S. Saha, *ACS Appl. Mater. Interfaces* **2020**, *12*, 40613–40619.
- [68] L. Sun, S. S. Park, D. Sheberla, M. Dincă, *J. Am. Chem. Soc.* **2016**, *138*, 14772–14782.
- [69] C. A. Farnandez, P. C. Martin, T. Schaefer, M. E. Bowden, P. K. Thallapally, L. Dang, W. Xu, X. Chen, B. P. McGrail, *Sci. Rep.* **2014**, *4*, 6114.
- [70] A. A. Talin, A. Centrone, A. C. Ford, M. E. Foster, V. Stavila, P. Haney, R. A. Kinney, V. Szalai, F. E. Gabaly, H. P. Yoon, F. Léonard, M. D. Allendorf, *Science* **2014**, *343*, 66–69.
- [71] S. Chen, J. Dai, X. C. Zeng, *Phys. Chem. Chem. Phys.* **2015**, *17*, 5954–5958.

Manuscript received: March 15, 2023

Accepted manuscript online: April 5, 2023

Version of record online: April 26, 2023